

# Evolutionary Status of the Pre-Protostellar Core L1498

T. B. Gil Kuiper, W. D. Langer, P. Velusamy

Jet Propulsion laboratory, California Institute of Technology, Pasadena, CA 91109

Received \_\_\_\_\_ accepted \_\_\_\_\_

# ABSTRACT

L1498 is a classic example of a dense cold pre-protostellar core. To study the evolutionary status, the structure, dynamics, and chemical properties of this core we have obtained high spatial and high spectral resolution observations of molecules tracing densities  $10^3$  to  $10^5 \text{ cm}^{-3}$ . We observed CCS,  $\text{NH}_3$ ,  $\text{C}_3\text{H}_2$ , and  $\text{HC}_7\text{N}$  with NASA's DSN 70 m antennas. We also present large scale maps of  $\text{C}^{18}\text{O}$  and  $^{13}\text{CO}$  observed with the AT&T 7 m antenna. For the high spatial resolution maps of selected regions within the core we used the VLA for CCS at 22 GHz, and the OVRO-M4A for CCS at 94 GHz and CS (2-1). The 22 GHz CCS emission marks a high density ( $n(\text{H}_2) > 10^4 \text{ cm}^{-3}$ ) core which is elongated with a major axis along the SE-NW direction.  $\text{NH}_3$  and  $\text{C}_3\text{H}_2$  emissions are located inside the boundary of the CCS emission.  $\text{C}^{18}\text{O}$  emission traces a lower density gas extending beyond the CCS boundary. Along the major axis of the dense core CCS,  $\text{NH}_3$  and  $\text{C}_3\text{H}_2$  emission show evidence of limb brightening. The observations are consistent with a chemically differentiated onion-shell structure for the L1498 core, with  $\text{NH}_3$  in the inner and CCS in the outer parts of the core. The high angular resolution ( $9''$  to  $12''$ ) spectral line maps obtained by combining NASA Goldstone 70 m and VLA data resolve the CCS 22 GHz emission in the southeast and northwest boundaries into arc-like enhancements, supporting the picture that CCS emission originates in a shell outside the  $\text{NH}_3$  emitting region. Interferometric maps of CCS at 94 GHz and CS at 98 GHz show that their emitting regions contain several small scale dense condensations. We suggest that the differences between the CCS, CS,  $\text{C}_3\text{H}_2$ , and  $\text{NH}_3$  emission are due to a time dependent effect as the core evolves slowly. We interpret the chemical and physical properties of L1498 in terms of a quasi-static (or slowly contracting) dense core in which the outer envelope is still growing. The growth

rate of the core is determined by the density increase in the CCS shell resulting from the accretion of the outer low density gas traced by  $C^{18}O$ . We conclude that L1498 could become unstable to rapid collapse to form a protostar in less than  $5 \times 10^5$  years.

*Subject headings:* star: formation - ISM: molecules - ISM: clouds -  
ISM: individual (L1498) -radio lines: ISM

## 1<sub>0</sub> INTRODUCTION

To analyze the structure and evolution of a prototype pre-proto-stellar core, we chose the dark cloud core L1498 in the Taurus complex, which is one of the smallest and simplest quiescent cores (cf. Benson & Myers, 1989). Its line width and size indicate that it is in an evolutionary stage potentially close to collapse. It is very cold with a kinetic temperature of 10 K (cf. Fiebig, 1990), or possibly as low as 6 K (Wolkovitch et al., 1996). It has one of the narrowest lines known,  $\sim 0.15 \text{ km s}^{-1}$  (Fuller & Myers, 1992; Velusamy et al., 1995). A multi-transition  $\text{C}_3\text{H}_2$  analysis (Cox et al. 1989) gave a gas density  $n(\text{H}_2)$  of  $8 \times 10^4 \text{ cm}^{-3}$  at the Benson & Myers reference position.

The physical condition and composition of the gas in L1498 are probably representative of that existing prior to star formation during the build-up of protostellar material. However, far from being simple, this source has proven to be quite enigmatic. A hint to its complexity emerged when the distribution of  $\text{CS}(2 \rightarrow 1)$  was found not to be coincident with the  $\text{NH}_3$  distribution (Zhou et al, 1989). Fiebig observed this core in several molecular species using the Effelsberg 100-m telescope with spatial resolution of  $40''$ . His CCS map at 22 GHz as well as maps at 45 and 94 GHz (Wolkovitch et al., 1996) show two local emission features separated by  $2''$ , while the  $\text{NH}_3$  map (Benson & Myers, 1989; Fiebig, 1990) shows a single component approximately midway between the CCS components. With higher angular resolution, Zhou et al (1994) observed a clumpy ring of  $\text{C}^{18}\text{O}(2 \rightarrow 1)$  emission with a hole centered approximately on the  $\text{NH}_3$  emission. Lemme et al (1995) found the ring-like structure less obvious in  $\text{C}^{18}\text{O}(1 \rightarrow 0)$ , rather more like the two component structure seen in CCS, but still recognizable when compared to the  $\text{C}^{18}\text{O}(2 \rightarrow 1)$  emission. In the  $\text{C}^{18}\text{O}(2 \rightarrow 1)$  transition, they also observed several small structures with sizes  $\sim 30''$  (0.02 pc) and masses  $\sim 0.01 M_\odot$ , comparable to the structures found by Langer et al (1995) in TMC1-D. Lemme et al (1995) concluded from studying  $\text{CS}(3 \rightarrow 2)$  emission maps in the

core that there was no evidence for inside-out collapse.

In this paper we extend the study of L1498 to smaller scales using single dish and interferometric observations. We recognize that part of the problem in interpreting the structures observed by different molecules is the chemical differentiation between tracer molecules. In order to resolve the chemical structure we present high spectral and spatial resolution observations of several high density tracer molecules, and in multiple transitions in the case of CCS. Our observations show that the dense core in L1498 is very inhomogeneous with large chemical variation. From the evidence presented here an overall picture emerges of a chemically differentiated multi-layered ellipsoidal shell structure for the core. The excitation analysis of CCS transitions are discussed by Wolkovitch et al. (1996). The physical characteristics of the small scale structures will be discussed in detail in Paper 11 (Langer et al, 1996). In this paper we discuss the overall chemical structure of L1498 and the status of its pre-protostellar evolution.

## 2. OBSERVATIONS

We made high spectral resolution observations of CCS, HC<sub>7</sub>N, and NH<sub>3</sub> at 22 GHz using NASA's Deep Space Network (DSN) 70 m antenna at Goldstone, and of C<sub>3</sub>H<sub>2</sub> with the DSN 70 m at Canberra. We mapped L1498 fully in CCS, but only along the elongated axis in C<sub>3</sub>H<sub>2</sub> and NH<sub>3</sub>, all with very high velocity resolutions of 0.008, 0.064, and 0.015 km s<sup>-1</sup>, respectively. We also observed the CCS transition at 45 and 94 GHz at the center position to obtain excitation information about CCS. In order to study the small scale structures in the features unresolved in the single dish maps, we selected a few fields for observation at very high spatial resolution using interferometers: 22 GHz CCS with the VLA, and 94 GHz CCS and 98 GHz CS with the OVRO-MMA.

The transitions observed and the telescopes used are described in Table 1. In Table

2 we list the rest, frequencies used for the spectra discussed in this paper. We also list the frequencies given in the literature in Table 2, many of these were taken from the JPL Spectral Line Catalog (Pickett, Poynter & Cohen, 1991). For CCS we have adopted the notation of Saito et al (1987) for labeling the levels.<sup>1</sup> Because of the high spectral resolution of our observations and the narrowness of the lines, uncertainties in the line rest frequencies can be significant. Therefore, in Table 2 we also give the corresponding uncertainty in  $V_{LSR}$ .

Among the transitions in Table 2, with the exception of  $\text{NH}_3$ , the frequency of the CCS ( $2_1 \rightarrow 1_0$ ) transition seems to be the most reliable. Therefore we have adjusted the rest frequencies of other transitions such that their  $V_{LSR}$  will match that of CCS ( $2_1 \rightarrow 1_0$ ) at the line peak as determined from a gaussian fit. Such an adjustment is valid because of the simplicity and the narrowness of the L1498 spectra. Indeed we suggest that these adjusted frequencies are to be preferred over the literature values. We found a systematic shift of the  $\text{HC}_7\text{N}$   $20 \rightarrow 19$  line in L1498 with respect to the other molecular lines. A similar shift was reported by Langer et al (1995) in TMC1. We used the  $\text{HC}_7\text{N}$  spectra in TMC1 and L1498 to recompute the frequency of this transition as 22559.9202 MHz with an accuracy of  $\pm 0.001$  MHz.

In Table 2 CS has the largest uncertainty in frequency. As pointed out by Snell, Langer, & Frerking (1982) the values used for CS may be in error. In the Pickett, Poynter & Cohen (1991) catalog, the frequency is given as  $97980.950 \pm 0.050$  MHz. The frequency used by Snell, Langer, & Frerking (1982) and Lemme et al (1995) is 97981.007 GHz. The OVRO-MMA observations use 97980.968 MHz. We used the CS (2-1) spectra from OVRO-MMA (this paper) and IRAM 30m (Langer et al. 1996) to estimate a new frequency

---

<sup>1</sup>The JPL catalog assigns a different labeling of (N,J) whereby the h' quantum number is assigned to the state of a given J which has the largest contribution from the basis function with the same N quantum number

that will be consistent with the CCS 22 GHz spectrum. We estimate the correct frequency for the CS (2-1) transition to be 97981.040 GHz within  $\pm 4$  kHz.

## 2.1. Single Dish Observations

Between 1993 October and 1994 November, we made single dish spectral line maps of L1498 in the 22 GHz CCS( $J_N=2_1 \rightarrow 1_0$ ) transition with 0.008 km s<sup>-1</sup> channel width, and with a high signal-to-noise ratio, Nyquist sampling every 24" over 4' x 5' region using the NASA Goldstone 70 m antenna. The observational details are given in Langer et al (1995). In November 1995 we made observations of the ( $J, K$ ) = (1,1) transition of NH<sub>3</sub> at 23.7 GHz using the same antenna, but with a new 18-26 GHz cooled-HFMT pre-amplifier in place of the maser. We used a velocity channel width of 0.0154 km s<sup>-1</sup> which is larger than that used for CCS in order to observe all of the 18 hyperfine lines of the ( $J, K$ ) = (1,1) transition within the available bandwidth. We observed 13 positions along the major axis every 20".

We also made observations of the [ $J_{K-,K+}=1_{1,0} \rightarrow 1_{0,1}$  transition] of C<sub>3</sub>H<sub>2</sub> at 18.3 GHz transition using the NASA Canberra 70-m antenna in September 1995. A cooled HFMT pre-amplifier covering 13-18 GHz was used. The downconverter is similar to the one at Goldstone. The signals were processed with a 16,384 channel digital fast Fourier spectrometer having a 20 MHz bandwidth. We mapped a 6' x 1.5' region along the major axis with Nyquist sampling every 25". We also set limits on the intensity of NH<sub>3</sub> (2,2) emission at three positions in L1498.

To get an overall view of the distribution of the less dense ( $11(11_2) < 10^4$  cm<sup>-3</sup>) regions in L1498 we also made large scale maps of <sup>12</sup>CO, <sup>13</sup>CO, and C<sup>18</sup>O emission with the AT&T Bell Laboratories 7m antenna. We mapped the <sup>12</sup>CO and <sup>13</sup>CO emission over a 12' x 12' region, and the C<sup>18</sup>O (1-0) emission over 8' x 8'. We used a velocity resolution of 0.068

$\text{km s}^{-1}$ .  $\text{C}^{18}\text{O}$  (1-0) spectra were also observed with a higher velocity resolution of  $0.034 \text{ km s}^{-1}$  at two positions corresponding to two peaks in CCS, in the SE and NW. The CCS 94 GHz and the  $\text{C}^{34}\text{S}$  (2-1) lines were also observed at the  $\text{NH}_3$  peak with the AT&T Bell Laboratories 7m antenna using a velocity resolution of  $\sim 0.039 \text{ km s}^{-1}$ .

## 2.2. Interferometric Observations

We used the VLA (I configuration) and the OVRO-MMA to study the small scale structure in the L1498 core. Due to limited observing time we were not able to map the entire extent of the core with the interferometers. Instead we selected a few fields based on the single dish CCS map at 22 GHz. The VLA CCS spectral line maps at 22 GHz were made in I-configuration on 1995 March 31 and April 7 for 12 hours total, with a velocity resolution  $\sim 0.04 \text{ km s}^{-1}$ . The data were taken using 256 channels and 0.78 MHz bandwidth without Hanning smoothing. The source 0400+258 was used for amplitude and phase calibration. The flux density of the calibrator was 0.63 Jy at 22 GHz and the radio source 3C48 was used for bandwidth calibration. The spectral line maps were produced using ALPS. To maximize the signal-to-noise ratio most of the maps were smoothed to a lower resolution of  $1.2''$ .

The CCS 94 GHz and CS 98 GHz OVRO-MMA spectral line maps were made between 1993 October and 1995 April. Our exploratory observations (93-94 observing season) used the five antenna array in the A configuration with the map center at  $\text{RA}(1950) = 04^{\text{h}}07^{\text{m}}50^{\text{s}}.0$  and  $\text{DEC}(1950) = 25^{\circ}02'1.2''$ , which is the position of the  $\text{NH}_3$  peak (Benson & Myers 1989). Both CCS and CS spectra were detected in the shortest baseline (15m). In CCS no small scale emission feature was detected within the field of view. In the case of CS no small structure was observed near the map center, and the only structure detected was located  $30''$  west of the map center. In our second set of observations in



1994 October-November we observed CS centered at this position and at a second position centered at the SE CCS peak in the single dish map. The results presented here are from this second set of observations which used the 6 antennas in configuration A. A third set of observations were made in 1995 April consisting of CCS at 94 GHz centered at two positions which were selected from our VLA maps of the CCS peak. All the OVRO data were taken using 128 channels with 1.98 MHz bandwidth without on-line Hanning smoothing (velocity resolution 0.05 km s<sup>-1</sup>). The source 0528+134 was used for both amplitude and phase calibration. The flux density of the calibrator was 4.9 and 5.2 Jy at 94 and 98 GHz, respectively. The data were calibrated using the OVRO-MMA software and the spectral line maps were produced using AIPS. The CS and CCS maps were smoothed to a 12'' beam to maximize their signal-to-noise ratio.

### 3. RESULTS

#### 3.1. Large Scale Velocity and Density Structure in L1498

We use our <sup>13</sup>CO and C<sup>18</sup>O (1-0) data to determine the large scale distribution of gas with low and moderate densities, respectively, in and around L1498. To illustrate the extent of the velocity field seen by different density tracers we show in Figure 1 examples of spectra observed at the CCS peak (RA(1950)=4<sup>h</sup>07<sup>m</sup>56<sup>s</sup>, DEC(1950)= 25 °01'30"). All the spectra except CS (2-1) are from the data reported in this paper. The CS (2-1) spectrum shown here was obtained by averaging IRAM 30 m data observed over a 1' extent centered at this position (Paper II). For these spectra we have adopted the rest frequencies listed in Table 2. The <sup>12</sup>CO and <sup>13</sup>CO spectra have very large line widths, extending from  $V_{LSR}$ = 7 to 10 km s<sup>-1</sup>. In contrast the HC<sub>7</sub>N spectrum shows the narrowest single velocity component at  $V_{LSR}$ =7.820±0.003 km s<sup>-1</sup> with FWHM=0.136±0.008 km s<sup>-1</sup>. C<sup>18</sup>O also shows strong

emission at this velocity. The presence of a second component at  $V_{LSR}=8.1$  km s<sup>-1</sup> is evident in the C<sup>18</sup>O (1-0) and CS (2-1) spectra. There is also some indication of this feature in the CCS spectra.

in order to bring out the velocity structure of the low density gas towards the direction of the dense core in L1498 we show in Figure 2 maps of <sup>13</sup>CO and C<sup>18</sup>O emission in three velocity ranges: 7.5 to 8.0, 8.0 to 8.5, and 8.5 to 9.0 km s<sup>-1</sup>. These maps also show a selected contour of the integrated 22 GHz CCS emission (see also Figure 3) to mark the location and extent of the high density core of L1498. Both the <sup>13</sup>CO and C<sup>18</sup>O maps show significant increase in the column density towards the core in the  $V_{LSR}$  range 7.5 to 8.0 km s<sup>-1</sup> although the <sup>13</sup>CO map may be affected by optical depth effects. The C<sup>18</sup>O map shows an elongated source approximately 8' x 5', with its minor axis at a position angle of  $\sim 30^\circ$  (E of N). The orientation and the extent of this emission seems to indicate that it comes from a larger volume surrounding the dense core traced by CCS. The low density gas in the velocity ranges 8.0 to 8.5 and 8.5 to 9 km s<sup>-1</sup> are located to the SE and NW, respectively, of the CCS core in both the C<sup>18</sup>O and <sup>13</sup>CO maps. It is not clear if these velocity features are related to the core or are only seen in projection. Here we limit our discussion to the structure of the dense core at 7.5 to 8.0 km s<sup>-1</sup>,

### 3.2. Single Dish Maps of the High Density Core

#### 3.2.1. DSN 70 m CCS Maps

To present an overview of the high density core of L1498 we first show the distributions of the integrated intensity and mean velocity of the 22 GHz CCS emission (Figure 3). CCS traces a roughly ellipsoidal distribution for the high density core with the major axis approximately along the southeast to northwest direction centered about 30'' SE of the

ammonia peak, which is labeled B. The CCS integrated intensity map additionally shows two distinct peaks labeled A and C. These peaks are connected by a ridge of fairly uniform CCS emission, roughly in the SE to NW direction. The  $\text{NH}_3$  peak is located slightly away from this ridge and appears to be in a region of low CCS emission. The velocity distribution in Figure 3b shows a gradient along the major axis of the core, perhaps indicating some rotation about a  $30^\circ$  position angle (east of north), or possibly due to an additional narrow velocity component in the SE part of the map (see below). The velocity shift is about  $0.05 \text{ km s}^{-1}$ , which amounts to  $0.42 \text{ km s}^{-1} \text{ pc}^{-1}$  over  $3'$  ( $0.12 \text{ pc}$ ).

Figure 4 shows the Goldstone 70 m channel maps of CCS emission at 22 GHz. Because of the high signal-to-noise ratio in the spectra, it was possible to make channel maps over a very narrow velocity range. The 70 m channel maps shown here were made in the exact channel frequencies and widths to match the VLA channels which were separated by 3 kHz ( $0.041 \text{ km s}^{-1}$ ). 1.1498 is recognized as an extended ( $\sim 4' \times 2.5'$ ) ellipsoidal component with a position angle of  $\sim 120^\circ$  and a velocity range of  $7.7\text{--}8.0 \text{ km s}^{-1}$ . Two features stand out within this distribution: 1) a prominent compact feature at its SE end has a velocity range of  $7.70\text{--}7.85 \text{ km s}^{-1}$ ; and 2) a weaker compact feature at the NE end ranges from  $7.75$  to  $7.9 \text{ km s}^{-1}$ .

### 3.2.2. Single Dish Spectra

In Figure 5 we show the single dish spectra of the high density tracer molecules CCS,  $\text{C}^{34}\text{S}$ ,  $\text{HC}_7\text{N}$ ,  $\text{C}_3\text{H}_2$ , and  $\text{NH}_3$  at the three representative positions marked A, B and C in Figure 3. For comparison we also show  $\text{C}^{18}\text{O}$ . The results of Gaussian fits of the line profiles are listed in Table 3. A close examination of the line intensities at the three positions in 1.1498 reveal large chemical differentiation within the core. There is an anticorrelation between the CCS and  $\text{NH}_3$  emission that is seen more clearly in these spectra. The largest

variation in the line intensities between positions A and B occurs for  $\text{NH}_3$  and  $\text{HC}_7\text{N}$ , but the strongest emission is at positions B and A respectively. We did not detect  $\text{NH}_3$  emission in the (2,2) transition with an upper limit of  $T_A < 0.1$  K.

in the case of  $\text{NH}_3$  our spectra included all 18 hyperfine lines of the (1,1) transition (Kukolich 1967). The observed spectrum consists of five groups of lines, separated by more than 7 km s<sup>-1</sup>. The central group, which is also the strongest, contains 8 of the hyperfine lines blended into two overlapping components. in the outer blue shifted group, the components overlap within the line width. The other three satellite groups consist of one bright line separated from a second weaker line by more than 0.3 km s<sup>-1</sup>. We used only these latter three groups because their structure makes it easier to fit the separate components. To determine the velocity and line-width of the ammonia emission we removed the weaker component in each of these pairs by a 'clean' procedure. This procedure successively subtracts components from the observed spectrum corresponding to the emission peak in the strongest line in each pair. Unlike the usual Gaussian fitting approach the intrinsic profile shape is preserved. The final spectra were obtained by averaging the line profiles derived from the three pairs. The averaged line profiles shown here are less subject to optical depth trapping effects because we did not include the central (strongest) component.

### 3.2.3. DSN 2'0 m $\text{NH}_3$ and $\text{C}_3\text{H}_2$ Position-Velocity Maps

To investigate further the chemical differentiation within the core, we also compared the large-scale distribution of  $\text{C}_3\text{H}_2$  ( $1_{1,0} \rightarrow 1_{0,1}$ ) and  $\text{NH}_3$  (1,1) emissions. The observations consisted of high resolution spectra spatially Nyquist sampled along the SE-NW major axis (at a position angle of 116°). In Figure 6 we show the position - velocity maps of  $\text{C}_3\text{H}_2$  and  $\text{NH}_3$  intensities. For a comparison we also show in Figure 6 the P-V map of CCS emission

at 22 GHz.

Figure 6 brings out remarkably well the velocity and spatial distributions of the emission from these molecules. The most striking feature is that all three molecules show distinctly different spatial extent but a common center.  $\text{NH}_3$  has the smallest extent, while CCS has the largest. The spatial extent of  $\text{C}_3\text{H}_2$  is somewhat between these two. All three maps show one strong peak and a shoulder extending to the opposite end. The observed distributions seem to be consistent with limb brightened emission at one end of the main axis. It is interesting that the strongest emission in CCS and  $\text{C}_3\text{H}_2$  is in the SE, in contrast to  $\text{NH}_3$  which peaks to the NW of this center. These distributions further suggest that the true center of the core is not the  $\text{NH}_3$  peak, but is displaced from it by about  $30''$  to the SE as marked in Figure 6. The emission of all three molecules along the major axis shows strong asymmetry about the center.

### 3.3. Interferometer Maps of Small Scale Structure

#### 3.3.1. VLA CCS Maps

To study the structure of this CCS emission at smaller scales we used the high spatial resolution capabilities of the VLA. The VLA field of view (primary beam  $\sim 2'$ ) is smaller than the size of the CCS core in 1,1498, and it was not possible to map it fully in the time available. Therefore we observed two fields along the major axis: one was centered at the SE emission peak seen in the single dish map near position A (Fig. 3a); the other field was at the opposite end near position C (Fig. 3a). In order to get a complete representation of the 22 GHz CCS emission channel maps, the VLA data for these fields were combined with the single dish Goldstone 70 m data. Figure 7 shows an example of the channel maps for  $7.80 \text{ km s}^{-1}$  obtained with 70 m alone, with the VLA, and combining the two. The reason

one needs to combine the data from the two maps is because the shortest spacing in the VLA was about  $2500 \lambda$  and hence, structures on the scale of  $30''$  and larger are missing in the VLA maps, as seen in Fig. 7b. On the other hand, the single dish 70 m map (Fig. 7a) contains all spatial frequencies up to about  $4000 \lambda$ . Hence by combining the VLA and 70 m data we are able to overcome some of the limitations of individual maps (see Fig. 7c). In the next paragraph we describe in more detail how we combined the two types of map data using AIPS.

First, all the single dish maps were attenuated by the VLA primary beam (FWHM of  $2''$ ) centered at the corresponding VLA map center. Then for each channel the visibilities at short spacings ( $<4000 \lambda$ ) were obtained by Fourier transforming the maps. We adopted the procedure suggested by Bajaja & van Albada (1979) and used the Gaussian beam size of  $45''$  to derive the spectral density function for the 70 m antenna. The visibilities derived from the single dish map were corrected by dividing them by the single dish spectral sensitivity function for the 70 m, and adjusting the relative weights of the single dish visibilities proportionately. These visibilities were then added to the VLA visibility data. The relative weights for the VLA and single dish visibilities were further adjusted by matching the overlapping region between  $2500$  and  $4000 \lambda$ . The channel maps were then made using the combined visibilities. The combined map reproduces the true brightness structure containing both small and large scale features, as seen in Fig. 7c. The combined maps were smoothed to a lower resolution to improve the signal-to-noise ratio. The beam used for the map in Fig. 7c is  $9'' \times 9''$ . However in view of the weakness of the emission in other channels we used a larger beam  $12'' \times 12''$  for all other channel maps discussed here.

The combined Goldstone-VLA channel maps for the two fields are shown in Fig. 8. The velocity spacing of the maps is  $0.04 \text{ km s}^{-1}$  which is less than the thermal line width of  $0.09 \text{ km s}^{-1}$  for CCS at 10 K. The top left panel shows the velocity integrated emission and the others are channels maps at the indicated  $V_{LSR}$ . In order to give an idea of the

full extent of the dense core at each velocity we also show a few representative contours of the corresponding single dish channel maps. In studying the two fields in the channel maps it should be borne in mind that they are not corrected for the 2' VLA primary beam and only the field within the 35 percent level of the primary beam is displayed. This taper of the VLA primary beam causes an apparent minimum in the region where the two fields overlap. A primary-beam-corrected 'mosaic' map will require at least an additional field near the center. Furthermore, the rms noise in the SE was only  $23 \text{ mJy(beam)}^{-1}$  while that in the NW field was higher  $33 \text{ mJy(beam)}^{-1}$  due to poor weather conditions. The most striking result in these maps are the small scale features (sizes  $\sim 20''$ ) that are resolved by the VLA. For example in the channel map at  $7.80 \text{ km s}^{-1}$  there are at least three features in the SE field and two in the NW.

The high resolution of the VLA has fully resolved the SE and NW brightest emission features in the single dish CCS map. The small scale features in the SE appear to lie along an arc which is best seen in Fig. 7c and in the  $7.80 \text{ km s}^{-1}$  channel map in Fig. 4, and it is also suggested by the single dish 70 m channel maps at  $7.80 \text{ km s}^{-1}$  and  $7.84 \text{ km s}^{-1}$ . The CCS emission along this arc is not uniform and consists of several small scale features. The southern ones appear to be slightly brighter than the northern components. In the NW field (at  $7.92 \text{ km s}^{-1}$ ) there is also a suggestion that the arc-like structure in the SE is mirrored at this end of the L1498 ellipsoid. However, this arc is less prominent than the one in the SE field, in part because of poorer signal-to-noise ratio. These arc-like structures are seen more clearly in the velocity integrated Goldstone-VLA map shown in Figure S. The enhanced CCS emission in the arcs along the SE and NW boundaries suggest that most of the CCS is distributed in an ellipsoidal shell, rather than uniformly throughout the core. The density traced by CCS in the single dish maps appears to be relatively constant as determined from CCS excitation analysis of three transitions (Wolkovitch et al. 1996), which would be consistent with a shell-like distribution.

### 3.3.2. 0 VRO-MMA CCS Maps

In order to search for higher density small scale features we also observed CCS ( $8_7 \rightarrow 7_6$ ) at 94 GHz with the OVRO-MMA in two fields along the eastern boundary, centered on the prominent emission peaks seen in the 22 GHz map at 7.80 km S-\* (Figs. 7 & 8). At 94 GHz, the most prominent emission is seen in the northern field while there is little emission in the southern field. Whatever emission is seen within the southern field of view corresponds to emission from the area that overlaps with the northern field of view. In other words, there appears to be no small-scale 94 GHz CCS emission in the southern component of the arc. Therefore, we present only the map of the northern field in Figure 9a. In Figure 9b we show the 94 GHz spectrum at the position of the CCS ( $8_7 \rightarrow 7_6$ ) peak. The details of the small scale structure and excitation modeling will be discussed in Paper 11. Here we only wish to point out that the location of the 94 GHz condensation appears to be associated with the limb brightened shell seen in the VLA map. The 94 GHz transition requires higher densities for excitation than the 22 GHz line (a critical density of  $5 \times 10^5$  versus  $3 \times 10^4 \text{ cm}^{-3}$ ) and therefore will trace high density condensations. The brightest 94 GHz emission is seen along and slightly inside of the northern part of the 22 GHz shell. The absence of any 94 GHz condensations further inward from the shell seems to indicate that the CCS abundance decreases, especially if the density increases inward, as would be expected for most cores.

### 3.3.3. 0 VRO-MMA CS (2-1) Maps

Figure 10a shows the map of CS (2-1) emission in the two fields mapped with the OVRO-MMA. These two fields are approximately centered on the southeast and northwest peaks in the 22 GHz CCS emission (Fig. 3). The maps were obtained by adding adjacent



channels over which the strongest emissions were seen. Figure 10b shows the CS(2-1) spectra at the brightest emission position in the two fields. The CS spectra are extremely narrow of the order of 2-3 channels or  $\sim 0.10$ -  $0.15 \text{ km s}^{-1}$ . The velocity difference between the SE and NW features is also consistent with the rotational velocity gradient observed in the single dish CCS emission maps (Figure 3b).

The prominent CS condensation seen in the SE field is about  $10'' \times 20''$  elongated north-south approximately perpendicular to the major axis of the CCS core. The second, weaker CS feature in the SE field does not correspond to any obvious feature in the CCS maps, but lies just east of the arc of CCS emission. Some of the faint features may be spurious, caused by side lobes as a result of missing some of the short spacings. Adding single-dish data to the OVRO observations will allow a more complete reconstruction and analysis of the CS emission. In the NW field, there is one bright feature (is seen at  $04^h 07^m 48^s, +25^\circ 02' 20''$ ). This feature appears to be spatially associated but not coincident with those seen in the 22 GHz CCS maps at  $7.80$  and  $7.84 \text{ km s}^{-1}$  (Figure 8). The arc described by the 22 GHz CCS emission appears to surround the CS (2-1) peak.

The physical and dynamical properties of the small scale structure will be discussed in Paper 11. Here we just wish to point out that the small-scale structure exhibits variation in both excitation and chemical composition. The most significant aspect of this structure is that the most prominent CS emission lies interior to the most prominent CCS emission at both the SE and NW ends of L1498. As discussed above the most prominent CCS emission appears to come from a roughly ellipsoidal shell which surrounds the brightest  $\text{NH}_3$  emission. Due to the limited field of view of the OVRO-MMA the CS (2-1) maps do not contain information about the overall distribution of CS in the core. It is interesting that the CS condensations observed with OVRO (which are presumably at higher densities than those in CCS at both 22 and 94 GHz) are located inside the CCS shell and yet outside the  $\text{NH}_3$  emission region (see below). No CS condensation was detected within a  $30''$  radius

of the nominal core center (given by Benson & Myers 1989) in the OVRO-MMA maps of the field centered on the  $\text{NH}_3$  peak (not shown here).

## 4. DISCUSSION

### 4.1. A Chemically Differentiated Shell Model

The picture of L1498 which emerges clearly from these observations is that of a clumpy ellipsoid with radial chemical differentiation outward from the center and an asymmetry between the east and west along its main axis. The evidence is re-capitulated in Figure 11, which shows the intensity of emission as a function of position along the major axis. The center of L1498 is located  $30''$  SE of the ammonia peak, which has hitherto been considered the center of the cloud. CCS,  $\text{C}_3\text{H}_2$ , and  $\text{NH}_3$  all are doubly peaked about this center. A similar bimodal distribution is implied by the CS interferometer data,  $\text{NH}_3$  is most closely confined to the center. This distribution is surrounded by  $\text{C}_3\text{H}_2$ , and possibly CS at a comparable distance from the center, and then CCS outside of that. These components are all embedded in a larger  $\text{C}^{18}\text{O}$  distribution.  $\text{C}_3\text{H}_2$ , CCS and CS are more prominent SE of the center, whereas  $\text{NH}_3$  has its main peak on the NW side.

The shell and core parameters are summarized in Table 4. The hydrogen density in the CCS shell was obtained from the excitation analysis of Wolkovitch et al. (1996). The density in the  $\text{NH}_3$  region was obtained using the approximations of Kuiper (1994), assuming a homogeneous sphere geometry and treating position B (Figure 3a) as the central line of sight. We used the collision cross-sections of Danby et al (1987). We assumed a kinetic temperature of 10 K and obtained an optical depth of  $1.5 \pm 0.5$  from the ratio of the integrated intensities of the inner satellite group to that of the central group. We found that the observed brightness temperature and optical depth imply a mean gas density of  $n(\text{H}_2)$

$>10^4 \text{ cm}^{-3}$ , which is consistent with the estimate of Benson & Myers. The result is very sensitive to beam filling factors, such as might be due to clumping, however, and increasing the observed brightness temperature by 60 percent (from the observed 3 K to 5 K) raises the density to  $> 5 \times 10^4 \text{ cm}^{-3}$ . Thus the actual density could be much higher. The mean density for  $\text{C}_3\text{H}_2$  was taken from Cox et al (1989). The density in the  $\text{C}^{18}\text{O}$  region was obtained from the brightness temperature. Assuming a  $\text{C}^{18}\text{O}$  abundance of  $1.6 \times 10^{-7}$  and a kinetic temperature of 10 K, we obtained an  $\text{H}_2$  column density of  $3 \times 10^{21} \text{ cm}^{-2}$  which, with a depth of 0.16 pc along the line of sight, implies a density of  $5 \times 10^3 \text{ cm}^{-3}$ . The densities in the core derived from our CCS and  $\text{NH}_3$  measurements are also consistent with those derived from CS by Lemme et al (1995). The gravitational mass of the core,  $M_{gr}$ , inside each of the boundaries traced by  $\text{NH}_3$ ,  $\text{C}_3\text{H}_2$ , CCS and  $\text{C}^{18}\text{O}$  is estimated from the densities above (see table 4).

#### 4.2. Chemical Evolution

Chemical differentiation in cloud cores can result from gradients in density, temperature, and the radiation field, because:

- (1) UV and visible radiation (both external and internal) photo-dissociate and ionize molecules;
- (2) the rates of gas phase reactions and depletion onto grains increase with density;
- (3) some reactions are temperature sensitive;
- (4) chemical evolution is explicitly time dependent; and,
- (5) mass transfer (a source term) introduces fresh material into the core.

We can rule out the first three as factors in the chemical variation in L1498. First, L1498 is an embedded quiescent core with no internal source and is well shielded. Second the temperature and density seem to vary little across the core. Excitation analysis of three

CCS transitions show that on the larger scale (single dish data) the temperature is in the range of 7 to 10 K. The center to edge variation in density is within a factor of 2 (Table 4). Although depletion onto grains make take place it does not explain the chemical differences in the core, because we expect  $\text{NH}_3$  should be depleted to the same extent as CS,  $\text{C}_3\text{H}_2$  (Bergin et al 1995), and presumably CCS (Table 4).

Therefore, the observed chemical differentiation is likely to be the result of mass transfer of fresh material. The absence of ammonia over this larger extent suggests that it represents a newly formed high density region, because the innermost region traced by  $\text{NH}_3$  emission is likely to contain a more evolved high density gas. As shown by Hirahara et al (1992) in TMC-1 and by Velusamy, Kuiper & Langer (1995) in B335, it appears that CCS is indeed a tracer of early time chemistry (dense gas formed recently  $t < 10^5$  yr), while  $\text{NH}_3$  is a tracer of more evolved gas. Hence, it is important to consider time dependent chemical effects while evaluating the structure of dense cores because not all features are observed at any given time by all molecular tracers.

#### 4.3. Growth Phase of a Pre-Protostellar Core

The chemical structure of 1,1498 seems to indicate that the dense gas near the central region traced by  $\text{NH}_3$  emission is more evolved than the outer gas traced by the CCS emission. One would expect to see such density and chemical structure in the case of a core undergoing an inside-out collapse as in the case of the protostellar infall envelope of B335 (Velusamy, Kuiper & Langer 1995), but the velocity and density structure of 1,1498 show no evidence for rapid contraction or collapse within the core.

We believe that 1,1498 is quiescent and pre-protostellar. No continuum emission was detected in our VLA or OVRO data in any of the fields. The  $5\sigma$  limit for detection was about 4 and 3 mJy at 22 and 94-98 GHz, respectively. While the 3 mm flux density limit is

an order of magnitude higher than what may be expected for cold dust emission in L1498 at these wavelengths (Ward-Thompson et al., 1994) it is consistent with the absence of a warm embedded, and hence evolved, source.

Table 4 shows the virial mass,  $M_{vir}$ , of the core inside various boundaries traced by  $\text{NH}_3$ ,  $\text{C}_3\text{H}_2$ ,  $\text{CCS}$  and  $\text{C}^{18}\text{O}$ . They were estimated using the formula given by MacLaren, Richardson & Wolfendale (1988). We used  $\Delta V$  corresponding to the thermal line width for molecular hydrogen at 10 K as the nonthermal pressure is negligible. As shown in Table 4, the dense core traced out to the  $\text{CCS}$  edge and the entire region traced by  $\text{C}^{18}\text{O}$  both appear to be close to virial equilibrium. Since  $M_{gr}$  for the  $\text{NH}_3$  core is only a lower limit, it is plausible, even likely, that it is also in virial equilibrium. As discussed in Section 3, the rotation of L1498 is less than  $0.4 \text{ km s}^{-1} \text{ pc}^{-1}$ , and therefore provides less than 10–3 of the total energy needed to support the cloud. We suggest that the L1498 core is contracting slowly (if at all), supported by thermal pressure and perhaps by magnetic fields, and is still far from the rapid collapse stage that marks protostar formation.

What mechanism other than inside-out-collapse can produce a newly formed high density envelope on the outside with an evolved dense gas on the inside closer to the center? We suggest that, while a very slow contraction may occur near the core center, the outer envelope of the dense core (as traced by  $\text{CCS}$ ) is still growing. In other words, chemically young high density gas is being formed at the interface between the high density  $\text{CCS}$  shell and the relatively low density ( $\sim 10^3 \text{ cm}^{-3}$ ) gas around it. A comparison of the  $\text{C}^{18}\text{O}$  and  $\text{CCS}$  line shapes (Figure 1 and Table 3) shows the presence of moderate density gas traced by  $\text{C}^{18}\text{O}$  (and perhaps  $\text{C}^{13}\text{O}$ ) with a larger velocity dispersion than that for the high density core traced by  $\text{CCS}$ . Lemme et al (1995) have also deduced a high degree of clumpiness in the low density gas traced by  $\text{C}^{18}\text{O}$ . It is, therefore, highly probable that some of these low mass clumps accrete onto the  $\text{CCS}$  core. As discussed in Langer et al (1995) for TMC-1, such coalescence may be an important part of the star formation process. We can estimate

a growth rate for the CCS core using the velocity dispersion in the CO spectra:

$$\dot{M}_{core} \sim m n A \Delta V_t/2$$

where  $m$  is the mean mass of a gas particle,  $n$  is the mean density of gas traced by  $C^{18}O$ ,  $A$  is the collisional cross section of the CCS core,  $\Delta V_t/2$  is the mean velocity with which the gas approaches the core, as deduced from the  $C^{18}O$  spectrum. The minimum value for  $A$  is given by the cross-sectional area of the CCS core. However, the actual impact parameter is larger due to gravity, and leads to a collision rate  $\simeq 2$  times larger. Another way to approximate this is to divide the surface area by two, since half the gas near the core surface moves towards it. Assuming a size of  $0.16 \times 0.10$  pc for the CCS core, a density of  $5 \times 10^3 \text{ cm}^{-3}$ , and  $\Delta V_t$  of  $0.4 \text{ km s}^{-1}$  for the surrounding gas, we estimate a growth rate of  $(1 - 2) \times 10^{-6} M_{\odot} \text{ yr}^{-1}$ . This suggests that the CCS shell with mass  $\sim 1 M_{\odot}$  is  $(0.5 - 1) \times 10^6$  yr old. The age of the  $NH_3$  core can be estimated from the total mass of the core to be  $(1.5 - 3) \times 10^6$  yr. The origin of the east-west chemical asymmetry is less obvious. It may be, however, that L1498 is accreting material more rapidly on that side, perhaps from the cloud which is seen in  $C^{18}O$  and  $^{13}CO$  (Figure 2).

From the plots of the line-width versus linear size for a collapse model (see Zhou et al 1994) it would appear that the L1498 core is on the verge of rapid collapse. From our mass estimates the L1498 core (as defined by the CCS boundary) appears to be close to gravitational stability. Its support is mainly thermal as the narrow line width of  $HC_7N$  indicates little turbulent pressure support. It would only require less than about  $1 M_{\odot}$  for the core to become unstable and collapse. At the estimated accretion rate this stage will be reached in less than  $10^6$  yrs.

## 5. SUMMARY

To study the structure, dynamics, and chemical properties of the L1498 core we have obtained high spatial and high spectral resolution observations of low, medium, and high density gas tracers. These include interferometric and single dish observations of the high density gas tracers CCS at 22 and 94 GHz, interferometric maps of CS (2-1), and large scale single dish  $C^{18}O$  (1-0) and  $^{13}CO$  (1-0) maps. The single dish CCS maps show an elongated structure with its axis at  $116^\circ$  position angle with the strongest emission in the SE. DSN 70 m observations of the  $NH_3$  and  $C_3H_2$  emission along this axis show a double peak spatial structure indicating limb brightening and are located within the boundary of the 22 GHz CCS emission. The true center of the core appears to be at the position of the local minimum between the  $NH_3$  peaks. The observations are consistent with a chemically differentiated onion-shell structure for the L1498 core, with  $NH_3$  and CCS in the inner and outer parts of the core, respectively. The high angular resolution ( $9''$  to  $12''$ ) 22 GHz spectral line maps obtained by combining NASA Goldstone 70 m and VLA data spatially resolve the CCS emission in the southeast and northwest boundaries into arc-like enhancements. These shapes support our picture that CCS emission originates in a shell outside the ammonia emitting region. The OVRO-MMA spectral line maps of CCS at 94 GHz and CS at 98 GHz in selected fields were made at ( $12''$ ) angular resolution and  $0.05 \text{ km s}^{-1}$  velocity resolution. The interferometric maps show that the emitting regions contain small dense condensations. These are located inside the boundary of the 22 GHz CCS emission which approximately delineates the  $104 \text{ cm}^{-3}$  boundary. Both CS and CCS are significantly diminished near the center.

The differences between the CCS, CS,  $C_3H_2$ , and  $NH_3$  emission suggest a time dependent evolution due to mass transfer and chemical evolution as the core evolves slowly. Obviously these show that time dependent chemical effects are important in evaluating

the structure of dense cores because not all features are observed at any given time by all molecular tracers. The CCS shell which contains newly formed dense gas shows evidence that the dense core in L1498 is still growing at the rate of  $\sim (1 - 2) \times 10^{-6} M_{\odot} \text{yr}^{-1}$ .

In conclusion, L1498 is a classic example of a dense cold pre-protostellar core that may be on the verge of rapid collapse to form a protostar. Our results suggest that it is in a quasi stable or slowly contracting phase. Its dense core is still growing by accreting the low density gas around it. We propose a new center for the core which is potentially the position where a protostar might form.

We thank the staffs of the Goldstone and Canberra complexes and particularly the Radio Astronomy and Radar Group for support of the 70 m observations. We thank Bob Wilson and Greg Wright for help with the observations at the AT&T Bell laboratories 7 m antenna. We thank R. Peng for helpful comments. Part of this research was conducted while 'I'. V. held a US National Research Council - Senior Resident Research Associateship. This work was performed at the Jet Propulsion Laboratory, California Institute of Technology, under contract with the National Aeronautics and Space Administration. The VLA of the National Radio Astronomy Observatory is operated by Associated Universities Inc. under contract, with the NSF. The OVRO millimeter array is supported by NSF grant AST 93-14079, the K. T. and E. L. Norris Foundation, and the JPL Director's Research Discretionary Fund.



## REFERENCES

- Bajaja, E. D. & van Albada, G. D. 1979, *A&A*, 75, 251.
- Benson, P. J. & Myers, P. C. 1989, *ApJS*, 71, 89.
- Bergin, E. A., Langer, W. D. & Goldsmith, P. F. 1995, *ApJ*, 441, 222.
- Cox, P., Walmsley, C. M., & Güsten, R. 1989, *A&A*, 209, 382.
- Danby, G., Flower, D. R., Valiron, P., Kochanski, E., Kurdi, I., & Dierksen, G. H. F. 1987, *J. Phys. B*, 20, 1039.
- Fiebig, I. 1990, Phil Thesis, Univ. Bonn (unpublished).
- Fuller, G. A. & Myers, P. C. 1992, *ApJ*, 384, 523.
- Hirahara, Y., Suzuki, H., Yamamoto, S., Kawaguchi, K., Kaifu, N., Ohishi, M., Takano, S., Ishikawa, S. & Masuda, A. 1992, *ApJ*, 394, 539.
- Kuiper, T. B. H. 1994, *ApJ*, 433, 712,
- Kukolich, S. G. 1967, *Phys. Rev.*, 156, 83.
- Langer, W. D., Velusamy, T., Kuiper, T. B. H., Levin, S., Olsen, E., & Migenes, V., 1995, *ApJ*, 453, 293.
- Langer, W. D., Velusamy, T., Kuiper, T. B. H., & Castets, A., 1996, in preparation, (Paper 11).
- Lemme, C., Walmsley, C. M., Wilson, T. L. & Muders, D. 1995, *A&A*, 302, 509
- MacLaren, I., Richardson, K. M., & Wolfendale, A. W. 1988, *ApJ*, 333, 821.
- Mathews, H. E. & Irvine, W. M. 1985, *ApJ*, 298, 1.61,

- Pickett, H., Poynter, R. & Cohen, E. 1991, Submillimeter, Millimeter and Microwave Line Catalog: revision 3. Jet Propulsion Laboratory.
- Saito, S., Kawaguchi, K., Yamamoto, S., Ohishi, M., Suzuki, H., & Kaifu, N. 1987, ApJ, 317, L115.
- Snell, R.L., Langer, W.D. & Frerking, M. A. 1982, ApJ, 255, 149.
- Velusamy, T., Kuiper, T. B. H., Langer, W. D., Levin, S. M. & Olsen, E. T. (1995). 2nd *Zermatt Conference on The Physics and Chemistry of Interstellar Molecular Clouds*, ed. G. Winnewisser & G. Pelz, (Springer-Verlog; Berlin) p. 136
- Velusamy, T., Kuiper, T. B. H. & Langer, W.D. 1995, ApJ, 451, L75.
- Ward-Thompson, D., Scott, P. F., Hills, R. E. & André, P. 1994, MNRAS, 268, 276.
- Wolkovitch, D., Langer, W. D., Goldsmith, P. F., and Heyer, M. 1996, (in preparation).
- Zhou, S., Wu, Y., Evans, N. J., II, Fuller, G. A. & Myers, P. C. 1989, ApJ, 346, 168.
- Zhou, S., Evans, N. J., II, Wang, Y., Peng, R. & Lo K. Y. 1994, ApJ, 433, 131.

Table 1: Transitions and Telescopes

Molecule	Transition	Band (GHz)	Antenna	HPBW (arcsec)	Velocity Resolution (km s <sup>-1</sup> )	Spatial' Resolution (pc)
Ccs	$J = 2_1 \rightarrow 1_0$	22	Goldstone 70m	45	0.008	0.030
CCS	$J = 4_3 \rightarrow 3_2$	45	Goldstone 34m	50	0.008	0.030
CCS	$J = 2_1 \rightarrow 1_0$	22	NRAO VLA	9	0.040	0.006
CCS	$J = 8_7 \rightarrow 7_6$	94	AT&T 7m	120	0.040	0.080
CCS	$J = 8_7 \rightarrow 7_6$	94	OVRO-MMA	9	0.052	0.006
HC <sub>7</sub> N	$J = 20 \rightarrow 19$	23	Goldstone 70m	45	0.050	0.030
CS	$J = 2 \rightarrow 1$	98	OVRO-MMA	9	0.049	0.006
C <sup>34</sup> S	$J = 2 \rightarrow 1$	96	AT&T 7m	115	0.034	0.068
C <sup>18</sup> O	$J = 1 \rightarrow 0$	110	"	1001	0.034	0.068
C <sub>3</sub> H <sub>2</sub>	$J_{K-,K+} = 1_{1,0} \rightarrow 1_{0,1}$	18	Canberra 70m	60	0.064	0.040
NH <sub>3</sub>	$J, K = 1, 1$	24	"	45	0.123	0.030
NH <sub>3</sub>	$J, K = 2, 2$	24	"	45	0.123	0.030

a. Spatial resolution calculated at the distance to L1498, 14 pc.

Table 2: Spectral line Frequencies<sup>a</sup>

Molecule	Transition	Frequency In Literature (MHz)	$V_{LSR}$ Uncertainty $\text{km s}^{-1}$	Frequency Used (MHz)
CCS	$J=2_1 \rightarrow 1_0$	$22344.033 \pm 0.001$	0.013	
CCS	$J=4_3 \rightarrow 3_2$	$45379.033 \pm 0.001$	0.013	
CCS	$J=8_7 \rightarrow 7_6$	$93870.107 \pm 0.020$	0.064	
HC <sub>7</sub> N	$J=20 \rightarrow 19$	$22559.907 \pm 0.009$	0.010	22559.920
CS	$J=2 \rightarrow 1$	$97980.950 \pm 0.050$	0.153	98981.040
C <sup>34</sup> S	$J=2 \rightarrow 1$	$96412.940 \pm 0.050$	0.153	
C <sup>18</sup> O	$J=1 \rightarrow 0$	$109782.182 \pm 0.008$	0.022	
C <sub>3</sub> H <sub>2</sub>	$J_{K-,K+} = 1_{1,0} \rightarrow 1_{0,1}$	$18343.145 \pm 0.002^b$	0.033	
NH <sub>3</sub>	$J, K = 1, 1$	$23694.49553 \pm 0.0001$	0.0013	23694.495
NH <sub>3</sub>	$J, K = 2, 2$	$23722.6333 \pm 0.0001$	0.0013	23722.633

a. It should be borne in mind that many programs used to compute Doppler shift may not have been verified at the 0.1  $\text{km s}^{-1}$  level of accuracy. The Doppler correction for the Goldstone was done with the DOPSET program obtained from NRAO. The software used to correct the Canberra data was based on NRAO's DOPSET but does not include the motion of the Earth around the Earth-Moon barycenter.

b. Matthews & Irvine (1985).

Table 3: Results of Gaussian Fits to Line Profiles

Transition		$T_A^*$	$V_{LSR}^a$	$\Delta V$
	GHz	K	km s <sup>-1</sup>	km s <sup>-1</sup>
Position A: (+78'', -42'')				
C <sup>18</sup> O	109	1.314 ± 0.011	7.874 ± 0.001	0.375 ± 0.003
CCS	22	1.8423 ± 0.020	7.8154 ± 0.001	0.190 ± 0.002
HC <sub>7</sub> N	22	0.3392 ± 0.016	7.820 ± 0.003	0.1364 ± 0.008
C <sub>3</sub> H <sub>2</sub>	18	2.215 ± 0.070	7.746 ± 0.004	0.260 ± 0.010
NH <sub>3</sub>	23	0.707 ± 0.023	7.821 ± 0.004	0.235 ± 0.010
NH <sub>3</sub> Peak: (+00'', +00'')				
CCS	22	1.457 ± 0.026	7.851 ± 0.001	0.1653 ± 0.003
CCS	93	0.872 ± 0.015	7.832 ± 0.002	0.1934 ± 0.004
HC <sub>7</sub> N	22	0.122 ± 0.015	7.866 ± 0.013	0.173 ± 0.031
C <sub>3</sub> H <sub>2</sub>	18	2.217 ± 0.089	7.801 ± 0.006	0.241 ± 0.015
NH <sub>3</sub>	23	2.504 ± 0.029	7.871 ± 0.010	0.221 ± 0.003
C <sup>34</sup> S	96	0.412 ± 0.011	7.8053 ± 0.003	0.226 ± 0.007
Position C: (-30'', +00'')				
C <sup>18</sup> O	109	1.374 ± 0.008	7.851 ± 0.001	0.298 ± 0.002
CCS	22	1.305 ± 0.027	7.846 ± 0.002	0.1793 ± 0.004
HC <sub>7</sub> N	22	0.125 ± 0.021	7.846 ± 0.015	0.1834 ± 0.036
C <sub>3</sub> H <sub>2</sub>	18	1.9724 ± 0.038	7.7944 ± 0.002	0.250 ± 0.005
NH <sub>3</sub>	23	1.592 ± 0.030	7.876 ± 0.004	0.2354 ± 0.011

a. Uncertainty based on fit alone.

Table 4: Parameters of the chemical shells in L1498 core<sup>a</sup>

Molecule	Size <sup>b</sup> (pc x pc)	Density $\text{cm}^{-3}$	$M_{\text{core}}(<R)^c$	
			$M_{\text{gr}}(M_{\odot})$	$M_{\text{vir}}(M_{\odot})$
C <sup>18</sup> O	0.28 x 0.16	5 X103	> 4	5 <sup>d</sup>
CCS	0.16 x 0.10	3 X104	3	3'
C <sub>3</sub> H <sub>2</sub>	0.13	5 X104	2 <sup>f</sup>	2 <sup>e,f</sup>
NH <sub>3</sub>	0.08	> 10 <sup>4</sup>	>0.1 <sup>f</sup>	1 <sup>e,f</sup>

a. Center of core at R.A. (1950): 04<sup>h</sup> 07<sup>m</sup> 52.0<sup>s</sup> and Dec. (1950): 25°02'00" <

b. The major and minor axis, at 30 percent of the peak.

c. The mass estimate corresponds to that within an oblate spheroid of semi-major axis R

d. Assuming 1/r density and  $AV = 0.45 \text{ km s}^{-1}$

e. Assuming uniform density and  $AV = 0.45 \text{ km s}^{-1}$

f. Assuming axial ratio same as for CCS

Fig. 1.- Single dish spectra at the CCS peak:  $RA(1950) = 4^h07^m56.0^s$ ,  $DEC(1950) = 25^\circ01'30''$ . The  $^{12}CO(1-0)$ ,  $^{13}CO(1-0)$  and  $C^{18}O(1-0)$  spectra are from the AT&T Bell Labs 7 m antenna. The CCS and  $HC_7N$  spectra at 22 GHz are from the DSN 70 m. The CS (2-1) spectrum is from IRAM 30 m smoothed to one arcmin resolution.

Fig. 2.- Channel maps of  $C^{18}O(1 \rightarrow 0)$  and  $^{13}CO(1 \rightarrow 0)$  emission, for  $V_{LSR}$  between 7.5 and 8.0 km S-l, 8.0 and 8.5 km S-l, and 8.5 and 9.0 km S-l. The first contours and contour intervals are 0.04 and 0.1 K km S-l, respectively, for  $C^{18}O$ , and  $^{13}CO$  maps. The grey levels in the  $^{13}CO$  maps mark intensities above 1 K km S-l. The thick contours represent the CCS emission at 22GHz in the velocity range 7.5 to 8.0 km s $^{-1}$  (see Figure 3).

Fig. 3.- Single dish CCS emission at 22 GHz observed with the DSN 70 m antenna. (a) integrated intensity. The labels A and C mark the CCS peaks, and B the  $NH_3$  peak. The first contour and contour interval are 0.03 K km s $^{-1}$ . (b) Mean  $V_{LSR}$ . The first (SE) and last (NW) contours are 7.810 and 7.870 km S-l respectively. Contour interval is 0.010 km s $^{-1}$ .

Fig. 4.- Channel maps of 22 GHz CCS emission obtained from the DSN 70 m data. The velocity of each channel is labeled. The velocity width of the channels is 0.04 km S-l. The spatial resolution is 45'' and the maps are Nyquist sampled. The first contour and contour interval are 0.2 K.

Fig. 5.- Single dish spectra of  $C^{18}O(1 \rightarrow 0)$ , CCS ( $2_1 \rightarrow 1_0$ ), CCS ( $8_7 \rightarrow 7_6$ ),  $C^{34}S(2 \rightarrow 1)$ ,  $HC_7N(20 \rightarrow 19)$ ,  $C_3H_2(1_{1,0} \rightarrow 1_{0,1})$ , and  $NH_3(1,1)$  at three representative position A, B and C in the core of L1498 as indicated in Figure 3.

Fig. 6----- Position-velocity maps of CCS, C<sub>3</sub>H<sub>2</sub>, and NH<sub>3</sub> taken with DSN 70-m antennas. The position offset is along the major axis (see Figure 3a). The velocity offset is with respect to  $V_{LSR} = 7.80$  km s<sup>-1</sup>. The first contours and contour intervals are 0.4, 0.4 and 0.2 K respectively for NH<sub>3</sub>, C<sub>3</sub>H<sub>2</sub> and CCS. Zero is at the nominal core center (Benson & Myers 1989). The dashed line shows the position 30" SE of the ammonia peak, which we suggest is the true center of 1,1498.

Fig. 7.- Channel maps of 22 GHz CCS emission of the 1,1498 core at  $V_{LSR} = 7.80$  km s<sup>-1</sup> and channel width 0.04 km s<sup>-1</sup> observed with (a) DSN 70 m, (b) VLA-D configuration, and (c) obtained by combining the 70 m and VLA data. The angular resolution in the VLA maps is 9". The beam sizes are indicated by the circle in the lower right corner of the maps. The contour intervals are 0.09, 0.26 and 0.35 K in T<sub>b</sub> respectively for the 70 m, VLA and combined maps. Note that prior to combining with the VLA data the 70 m map was attenuated by the VLA primary beam (2') and the VLA and combined maps shown here are not corrected for primary beam.



Fig. 8--- Channel maps of 22 GHz CCS emission made by combining the DSN 70 m and VLA data. The contours and grey levels show the two fields observed with the VLA: (i) the southeast field centered at the position  $RA(1950) = 04^h07^m56^s.0$ ;  $DEC(1950) = 25^\circ 01'45''$ . (ii) the northwest field centered at the position  $RA(1950) = 04^h07^m47^s.5$ ;  $DEC(1950) = 25^\circ 02'12''$ . The maps are not corrected for primary beam attenuation. The intensities are averaged over four adjacent channels covering  $0.16 \text{ km s}^{-1}$  centered at  $V_{LSR} \sim 7.75 \text{ km s}^{-1}$ . Only intensities inside the 35 percent level of the primary beam are plotted. The thick contours represent the 1, 2 and 3 K levels of the single dish 70 m CCS 22 GHz emission at the corresponding velocity. The velocity of each channel is labeled. The velocity width of the channels is  $0.041 \text{ km s}^{-1}$ . The spatial resolution in the maps is  $12'' \times 12''$ . The lowest contour level and contour interval are  $45 \text{ mJy beam}^{-1}$  ( $0.76 \text{ K in } T_b$ ). The rms noise in the southeast and northwest fields are 23 and 33  $\text{mJy beam}^{-1}$  respectively. The top left panel shows the integrated intensity. The first contour and contour levels are 0.015 and  $0.008 \text{ km s}^{-1} \text{ mJy (beam)}^{-1}$ .

Fig. 9--- (a) Map of 94 GHz CCS emission made with the OVRO-MMA data for the field centered at the position  $RA(1950) = 04^h07^m56^s.0$ ;  $DEC(1950) = 25^\circ 01'45''$ . The map is not corrected for primary beam attenuation. The intensities are averages of three adjacent channels. Only intensities inside the 35 percent level of the primary beam are plotted. The thick contour represents the 50 and 75 percent levels of the single dish 70 m CCS 22 GHz emission. The spatial resolution in the maps is  $12'' \times 12''$ . The lowest contour level and contour interval are  $35 \text{ mJy beam}^{-1}$  ( $0.34 \text{ K in } T_b$ ). (b) The 94 GHz CCS spectrum of the brightest emission feature, with linewidth of  $0.168 \text{ km s}^{-1}$ .

Fig. 10--- (a) Maps of CS (2-1 ) emission made with the OVRO-MMA data in two fields: (i) the eastern field centered at  $RA(1950)=04^h07^m56^s.0$ ;  $DEC(1950) = 25^\circ 01'30''$ , and (ii) the western field centered at  $RA(1950)=04^h07^m48^s.0$ ;  $DEC(1950)= 25^\circ 02'12''$ . The intensities are averages of three adjacent channels covering  $0.15 \text{ km s}^{-1}$  at  $V_{LSR} \sim 7.80 \text{ km s}^{-1}$ . The maps are not corrected for primary beam attenuation. Only intensities inside the 35 percent level of the primary beam are plotted. The thick contours represent 50 and 75 percent levels of the single dish 70 m CCS 22 GHz emission. The intensities are average of three adjacent channels. The spatial resolution in the maps is  $12'' \times 12''$ . The lowest contour level and contour interval are  $35 \text{ mJy beam}^{-1}$  ( $0.31 \text{ K in } T_b$ ). (b) CS (2-1) spectra of the brightest emission features in the SE and NW fields. Note the narrow linewidths,  $\sim 0.10$  to  $0.15 \text{ km s}^{-1}$ .

Fig. 11.- Comparison of spatial distribution CCS, CS,  $C_3H_2$ , and  $NH_3$ . The intensities integrated from 7.7 to 7.9  $\text{km s}^{-1}$  are plotted as a function offset along the major axis (see Figure 3a). Zero offset is at the nominal core center. The vertical axis indicates the position of the true center.

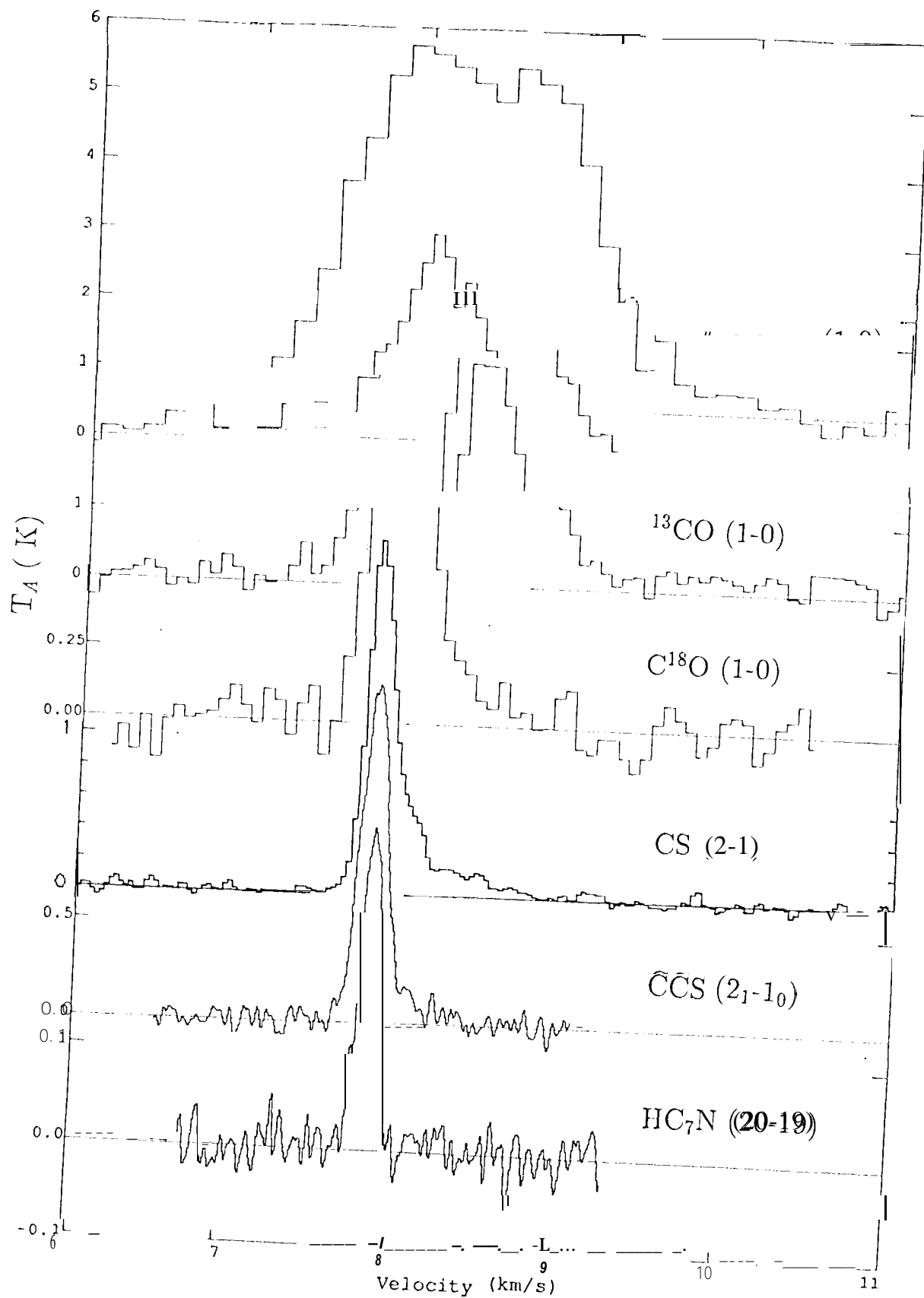


Fig. 1

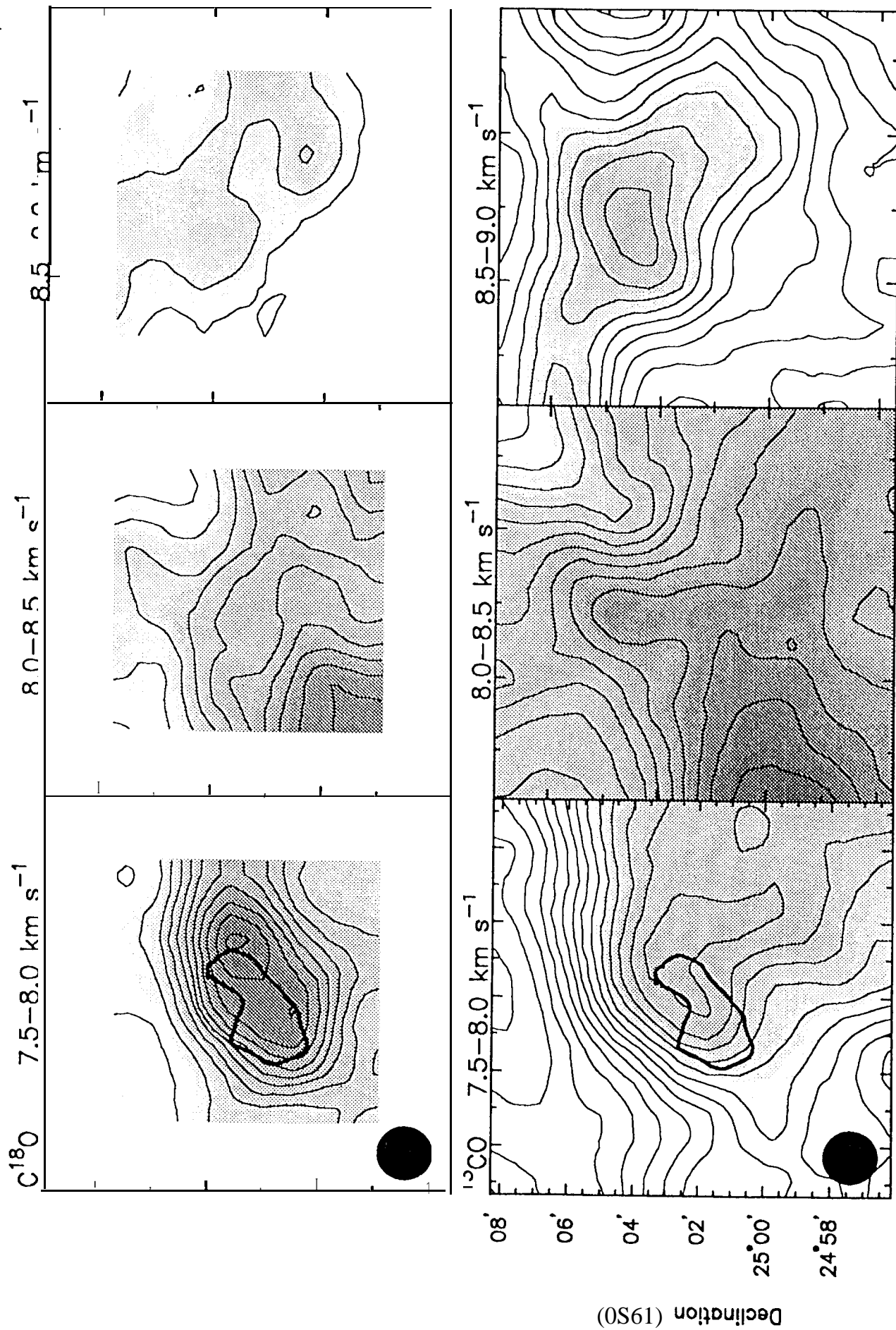


Fig. 2.

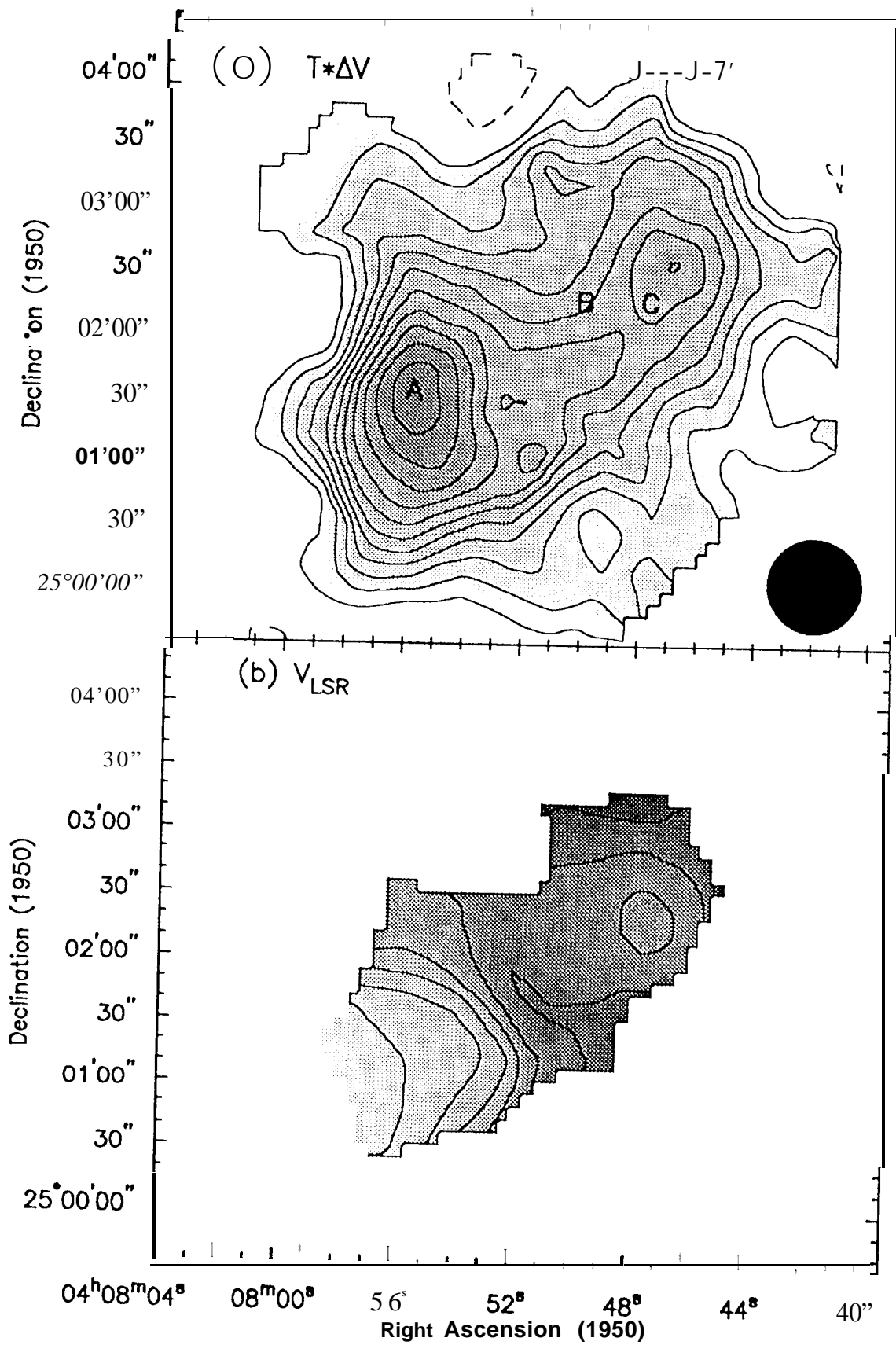


Fig. 3

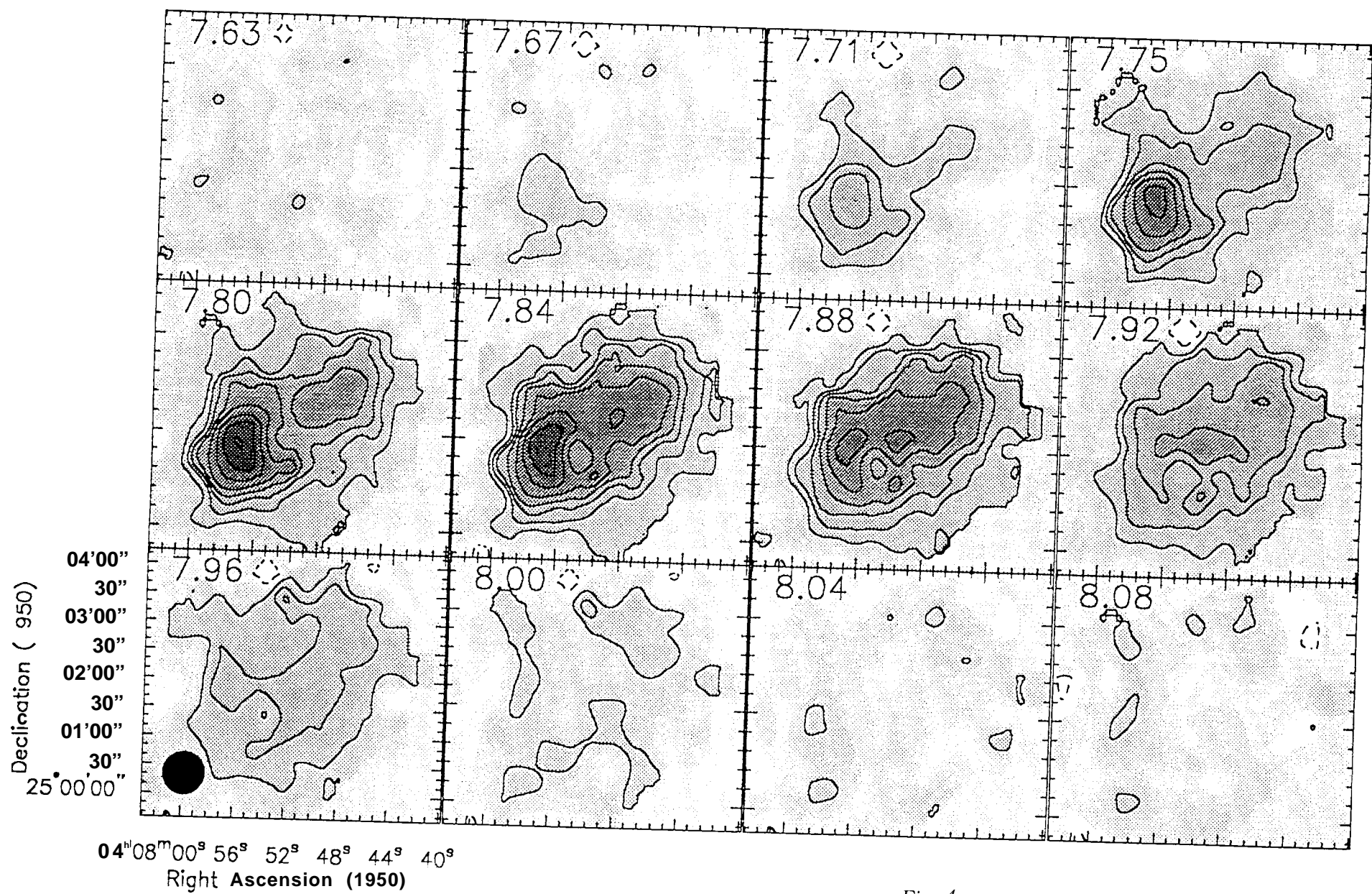
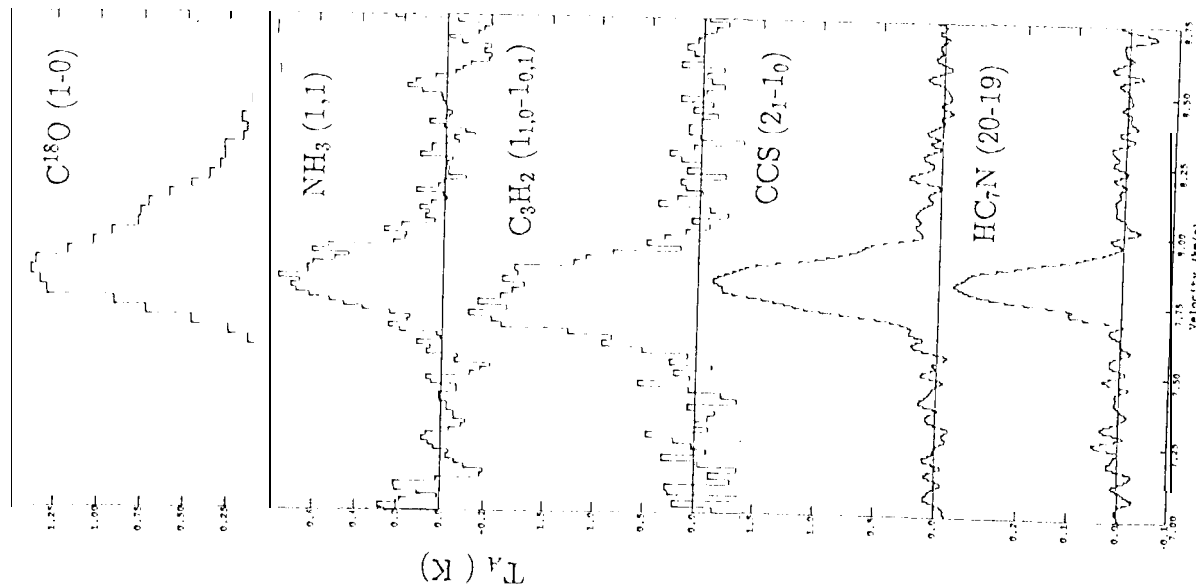
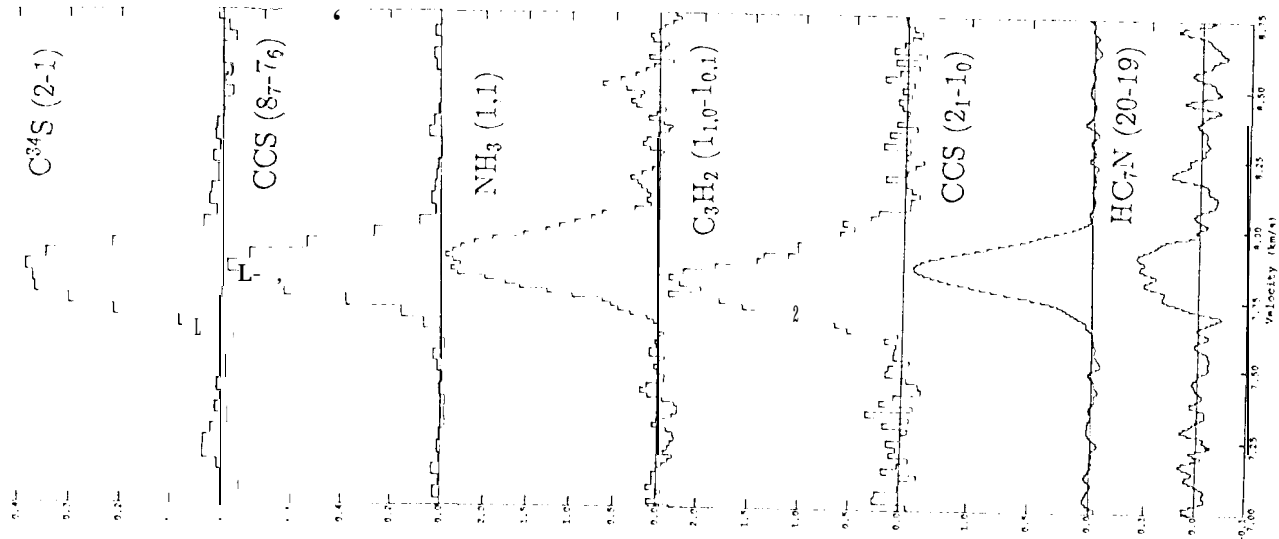


Fig. 4

# POSITION A



# POSITION B



# POSITION C

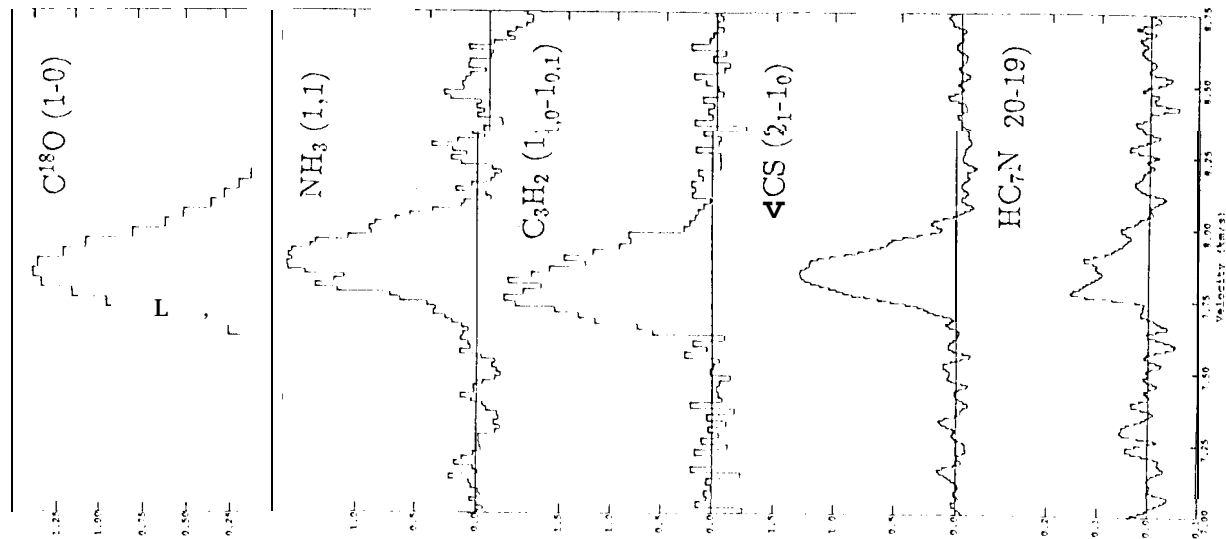


Fig. 5

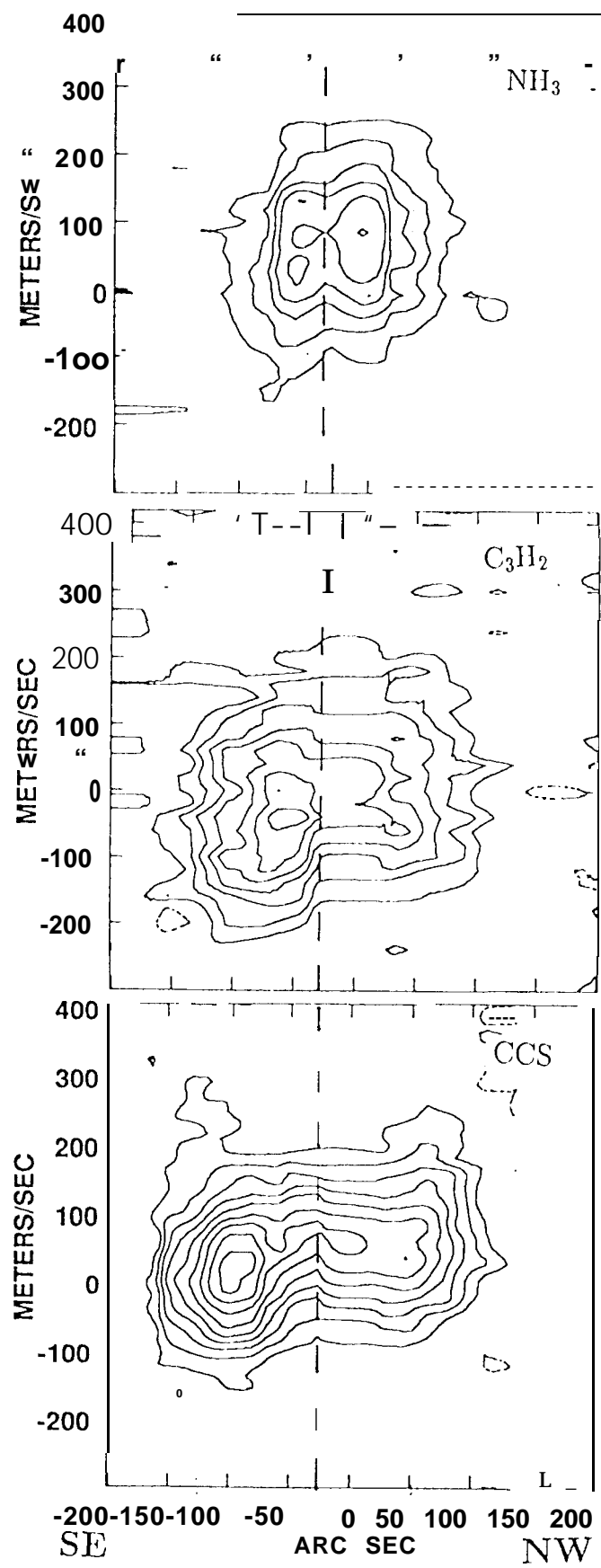


Fig. 6



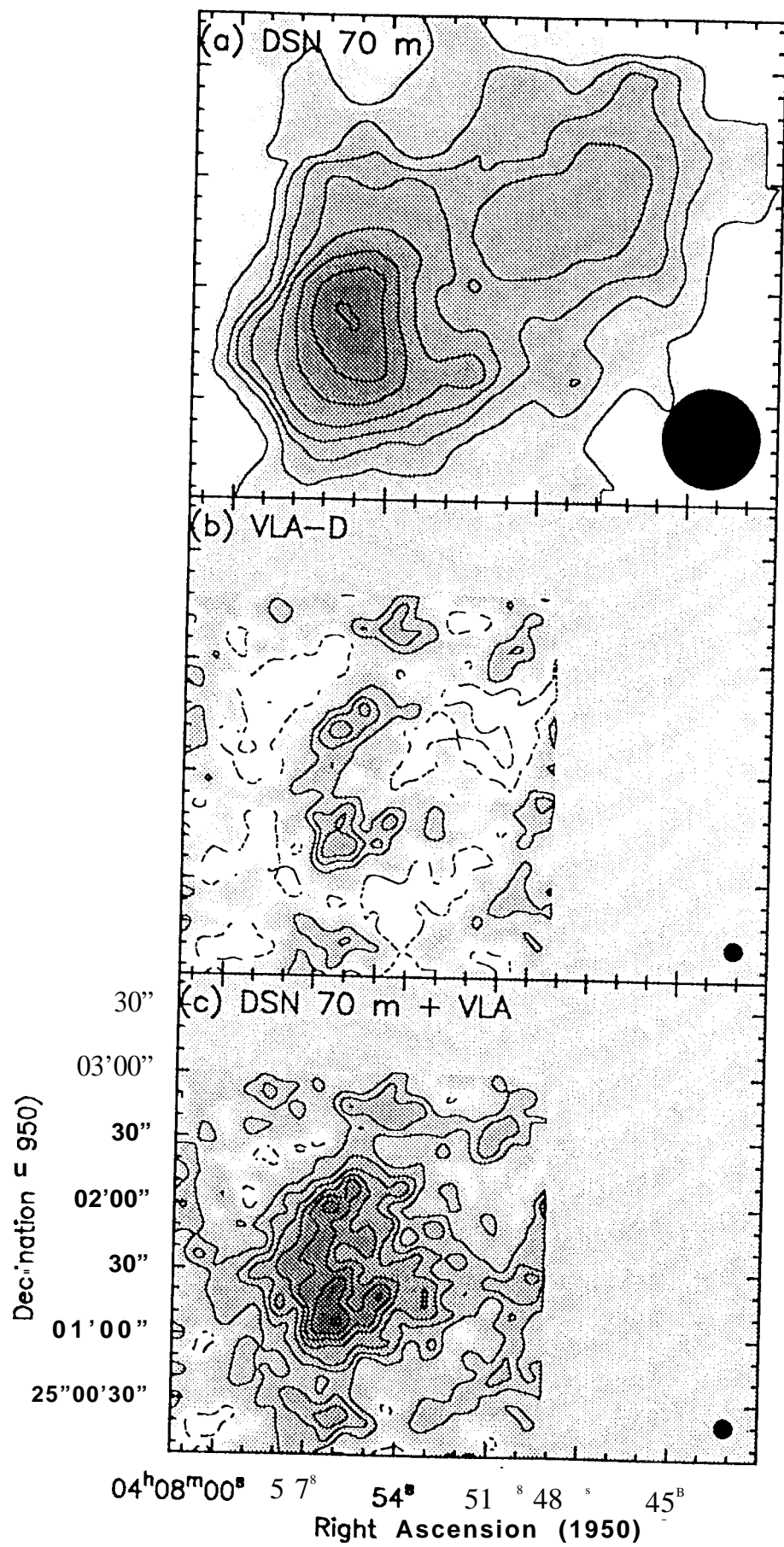


Fig. 7



Fig. 8

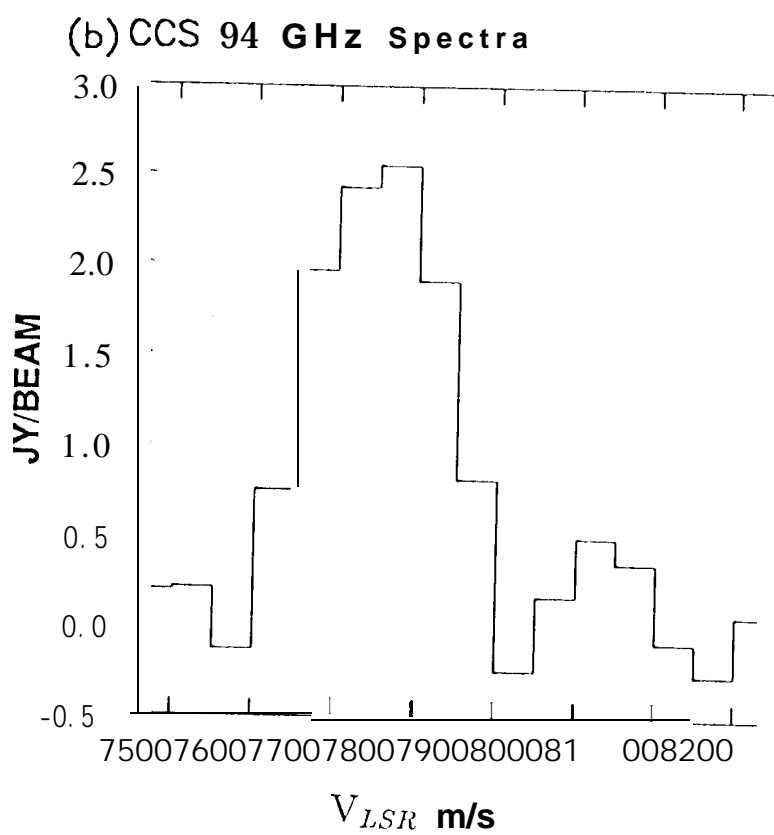
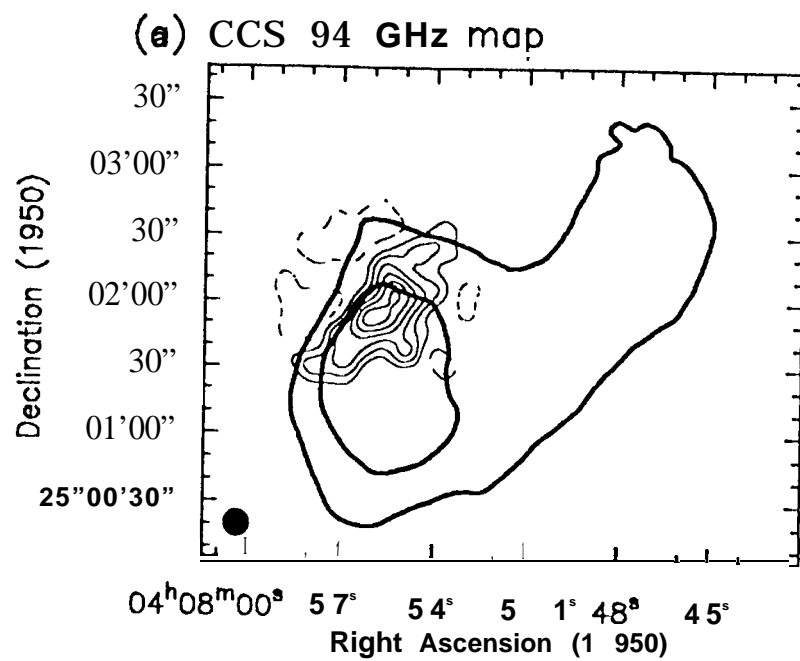


Fig. 9

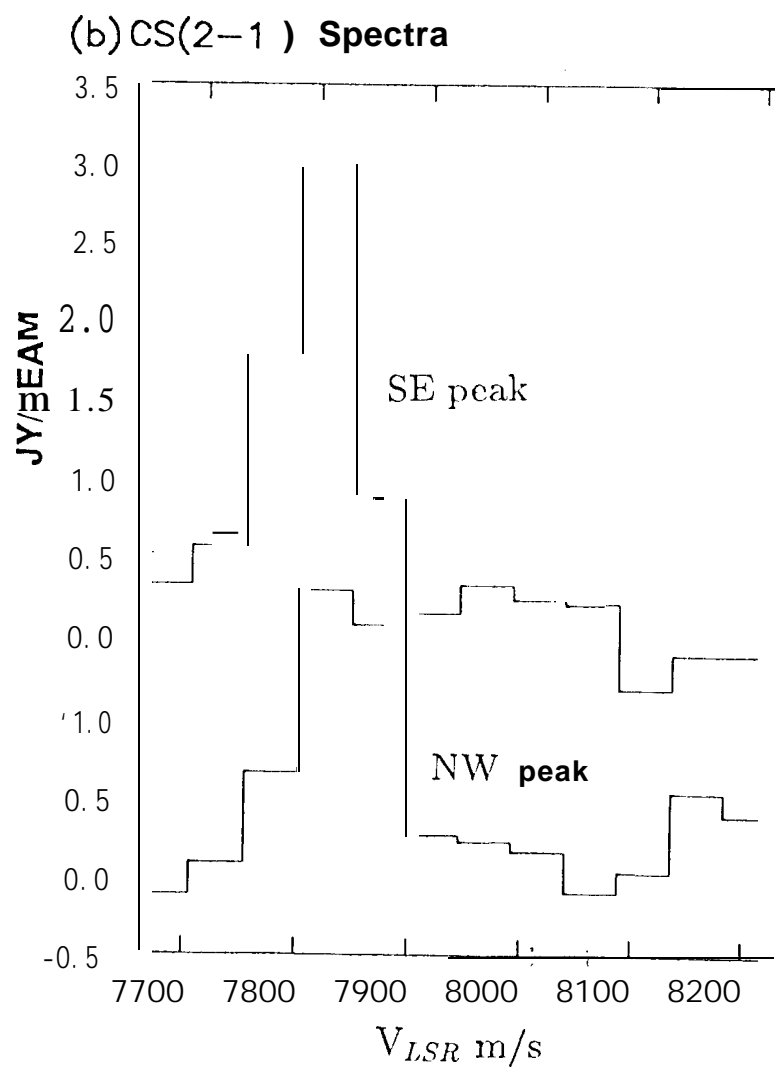
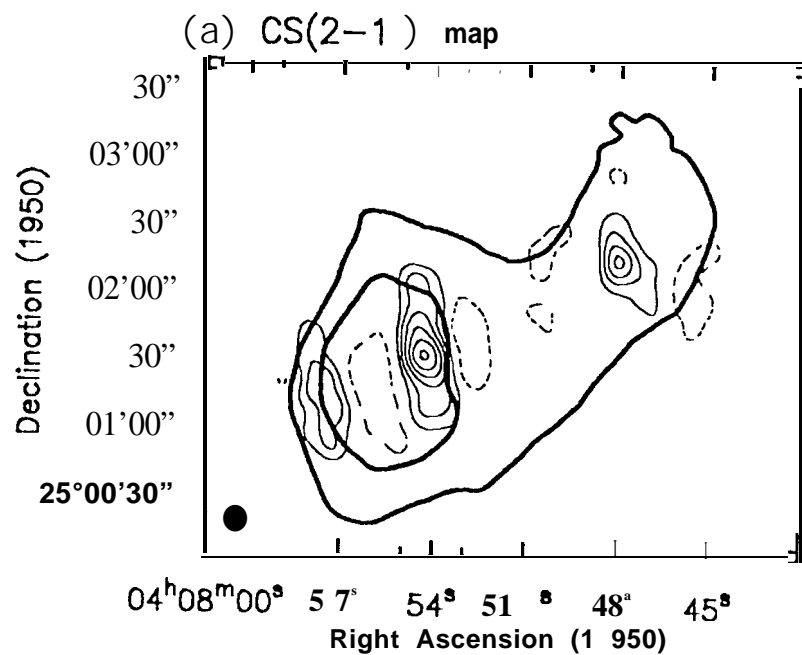


Fig. 10

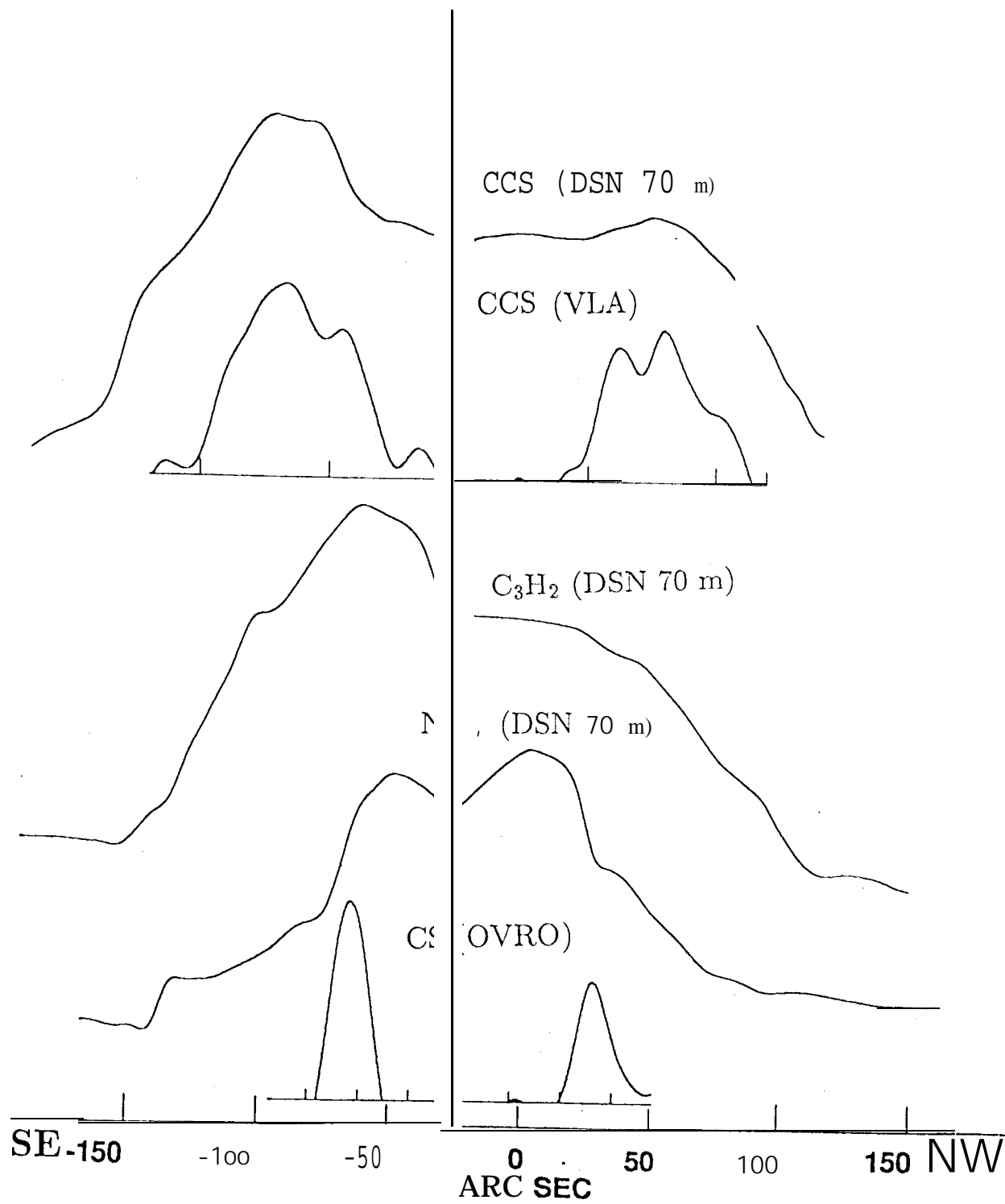


Fig. 11